Commun. Comput. Phys.
doi: 10.4208/cicp.151214.250515s

Vol. **18**, No. 4, pp. 1072-1094
October 2015

Direct-Forcing Immersed Boundary Method for Mixed Heat Transfer

Ming-Jyh Chern[1], Dedy Zulhidayat Noor[2], Ching-Biao Liao[3] and Tzyy-Leng Horng[4,*]

[1] *Department of Mechanical Engineering, National Taiwan University of Science and Technology, Taipei, Taiwan.*
[2] *Department of Mechanical Engineering, Institut Teknologi Sepuluh Nopember Sukolilo, Surabaya, Indonesia.*
[3] *Department of Water Resources Engineering and Conservation, Feng Chia University, Taichung, Taiwan.*
[4] *Department of Applied Mathematics, Feng Chia University, Taichung, Taiwan.*

Received 15 December 2014; Accepted (in revised version) 25 May 2015

Abstract. A direct-forcing immersed boundary method (DFIB) with both virtual force and heat source is developed here to solve Navier-Stokes and the associated energy transport equations to study some thermal flow problems caused by a moving rigid solid object within. The key point of this novel numerical method is that the solid object, stationary or moving, is first treated as fluid governed by Navier-Stokes equations for velocity and pressure, and by energy transport equation for temperature in every time step. An additional virtual force term is then introduced on the right hand side of momentum equations in the solid object region to make it act exactly as if it were a solid rigid body immersed in the fluid. Likewise, an additional virtual heat source term is applied to the right hand side of energy equation at the solid object region to maintain the solid object at the prescribed temperature all the time. The current method was validated by some benchmark forced and natural convection problems such as a uniform flow past a heated circular cylinder, and a heated circular cylinder inside a square enclosure. We further demonstrated this method by studying a mixed convection problem involving a heated circular cylinder moving inside a square enclosure. Our current method avoids the otherwise requested dynamic grid generation in traditional method and shows great efficiency in the computation of thermal and flow fields caused by fluid-structure interaction.

AMS subject classifications: 74F10, 65M06, 76D05

Key words: Direct-forcing immersed boundary method, fluid-structure interaction, mixed convection.

*Corresponding author. *Email address:* tlhorng123@gmail.com (T.-L. Horng)

 ©2015 Global-Science Press

https://doi.org/10.4208/cicp.151214.250515s Published online by Cambridge University Press

Nomenclature

A dimensionless amplitude
d dimensionless displacement
D dimensionless diameter
$\mathbf{f}$ virtual force
$\mathbf{F}$ total force acting on a solid body
H total heat transfer over body surface
L dimensionless length
n normal direction
$\overline{\text{Nu}}$ average Nusselt number
p dimensionless pressure
P dimensionless parameter
Pr Prandtl number
q virtual heat source
r dimensionless gyration radius
R dimensionless radius
Ra Rayleigh number
Re Reynolds number
St Strouhal number
t dimensionless time
T temperature, K
$\mathbf{u}$ dimensionless velocity
V volume of a solid object
W dimensionless area
x,y horizontal and vertical cartesian coordinate
x_r dimensionless recirculation length

Greek symbols

η volume of solid (VOS)
ϖ non-dimensional oscillation angular frequency, $\omega D/u_s$
ω oscillation angular frequency, s^{-1}
θ non-dimensional temperature
α thermal diffusivity

Superscript

m time step level

Subscripts

f fluid
s solid
x Position

1 Introduction

Fluid-structure interactions are common phenomena in flow physics and heat transfer problems, e.g. a uniform flow past cylinders and wind past rotating blades. Simulations of fluid-structure interactions are challenging and difficult. First of all, the configuration of a structure is often complex, so a distorted or unstructured grid is necessary. In addi-

https://doi.org/10.4208/cicp.151214.250515s Published online by Cambridge University Press

tion, given that the solid structure moves or rotates, grids will have to be re-generated due to the movement of the solid structure. The flow and heat transfer in a jet engine is a typical fluid-structure interaction problem. Air enters to the engine and flows past a series of rotating blades and stators. Fuel is burned and combustion occurs in the engine, so heat is generated and transmitted by the products of combustion to the rotating blades. Simulations of the air flow and heat transfer in the jet engine become difficult due to the complex configuration of the passageway and fast rotating blades. That is, the fluid domain always changes and its mesh generation is costly.

To predict fluid-structure interactions accurately, a variety of computational methods have been proposed. The most common method to simulate the flow with a complicated solid boundary is to use a body-fitted technique with grids fitting and clustering along the complex boundary. Most of time, the solid object may not be at rest and it requires further technique to deal with a moving object. The Arbitrary Lagrangian Eulerian (ALE) numerical method is a popular approach to accommodate the complicated fluid-structure interface varying with time. In the Eulerian coordinate frame, fluids flow through the static computational mesh. While in the Lagrangian coordinate, the mesh moves with the solid. Arbitrary Lagrangian-Eulerian (ALE) methods introduced by Hirt *et al.* [1] appear to be a reasonable compromise between Lagrangian and Eulerian approaches. The ALE method consists of several Lagrangian computational time steps followed by a mesh rezoning and a conservative quantities remapping. The mesh rezoning step smoothes the Lagrangian computational mesh and avoids its distortion. During the remapping step the conservative quantities are conservatively remapped from the old Lagrangian mesh to the new smooth one. After remapping the Lagrangian computation continues until the next rezone/remap steps which introduce the Eulerian flavor into the method allowing mass flux between computational cells. The rezone/remap steps keep the quality of the moving mesh good enough during the whole computation and are performed either regularly after fixed amount of Lagrangian time steps or when mesh quality deteriorates under some threshold. Many scholars have described ALE strategies to optimize accuracy, robustness, or computational efficiency [2–6]. Nevertheless, mesh updating or re-meshing is computationally expensive for the ALE algorithm.

In addition to the ALE algorithm, the immersed boundary method is becoming popular since it was first introduced by Peskin [7] due to its capability to handle simulations for a moving complex boundary with lower computational cost and memory requirements than the conventional body-fitted method. In this method, a fixed Cartesian grid and a Lagrangian grid are employed for fluids and immersed solid object, respectively. The interaction between fluids and the immersed solid boundary is linked through the spreading of the singular force from the Lagrangian grid to the Cartesian grid and the interpolation of the velocity from the Cartesian grid to the Lagrangian grid using a discrete Dirac delta function. Furthermore, some modifications and improvements of this method have been proposed by other researchers [8–11]. This method can be categorized as a continuous forcing method in which a forcing term is added to the continuous Navier-Stokes equations before they are discretized.

https://doi.org/10.4208/cicp.151214.250515s Published online by Cambridge University Press

Instead of using a delta function to distribute force from the Lagrangian grid to the Cartesian grid, Mohd-Yusof [12] introduced a novel immersed boundary method, namely the direct-forcing immersed boundary method (DFIB). This method uses a virtual forcing term determined by the difference between the interpolated velocities at the boundary points and the desired boundary velocities. This method is also known as a discrete forcing method since the forcing is either explicitly or implicitly applied to the discretized Navier-Stokes equations. The idea of DFIB has been used and developed successfully in many applications [13–20]. An impressive example is the famous work by Fadlun *et al.* [14] who developed a model combining the immersed boundary method and the finite difference method for three dimensional complex flow simulations. Some cases including the flow inside an IC piston/cylinder assembly at high Reynolds number were simulated successfully. The major issue of their work is the extrapolation of fluid velocity near solid-fluid interface into the interior of solids via virtual force to uphold the no-slip boundary condition at solid-fluid interface in order to obtain the second-order accuracy in space.

For immersed boundary methods applied to heat transfer problem, Paravento *et al.* [21] introduced an immersed boundary method for heat convection problems. They solved both a hot and insulated square body located in a 2D channel. Nevertheless, if an irregular solid object is considered in their immersed boundary model, then interpolations will be required and consequently, the advantage of their immersed model will not exist. Vega *et al.* [22] proposed a general scheme for the boundary conditions in convection and conduction heat transfer using an immersed boundary method. The momentum and energy forcing terms are imposed into momentum and energy equations followed by the projection method to uphold the divergence free condition in a non-staggered grid configuration. Some cases regarding heat conduction, forced and natural convection were simulated and validated with success. Pan [23] introduced an immersed boundary method on unstructured Cartesian meshes for incompressible flows with heat transfer. The solid body is identified by a volume-of-body (VOB) function analogous to the volume-of-fluid (VOF) function. This VOB approach can also be applied to the energy equation with a Dirichlet boundary condition.

In this present work, we apply DFIB with some modifications to simulate fluid-structure interactions with mixed heat transfer (forced and natural heat convection). The solid object immersed within a flow field can be denoted by the volume of solid (VOS) function η, which is defined as the volume fraction of solid in a cell. A cell fully occupied by solids will be denoted as $\eta = 1$, while the one fully occupied by fluids will be $\eta = 0$. A cell occupied partly by fluids and solids, commonly called a cut cell, will have a fractional η then. η in a cut cell sure can be determined accurately by studying how the solid boundary cuts the cell. However, a more efficient way is to resolve the designated Cartesian mesh to a finer one, and count the box number occupied by solids in an original designated cell. The fraction of solid box number to the total box number in an original cell will be a good approximation of η for that original cell. The momentum and energy equations for fluids are solved simultaneously with extra virtual forcing and energy

https://doi.org/10.4208/cicp.151214.250515s Published online by Cambridge University Press

source terms for a solid regime to achieve desired boundary conditions on fluids imposed by solids. Numerical details will be described in the following section and several flow and heat transfer problems involving a moving body are computed to demonstrate the capability of the present scheme in handling fluid-solid interactions with heat transfer.

2 Mathematical formulae and numerical methods

2.1 The governing equations

The continuity, momentum and energy conservation laws are used as the governing equations for fluid flows. A Newtonian fluid is considered in this study. The Boussinesq approximation for the buoyancy due to the density variation of a fluid is employed. The governing equations for an incompressible Newtonian fluid are expressed in the following non-dimensional forms:

$$\nabla\cdot\mathbf{u}=0, \tag{2.1}$$

$$\frac{\partial\mathbf{u}}{\partial t}+\nabla\cdot(\mathbf{uu})=-\nabla p+P_1\nabla^2\mathbf{u}+\eta\mathbf{f}-P_2\theta\mathbf{e}_z, \tag{2.2}$$

$$\frac{\partial\theta}{\partial t}+\nabla\cdot(\mathbf{u}\theta)=P_3\nabla^2\theta+\eta q, \tag{2.3}$$

where $\mathbf{u}$, p and θ are non-dimensional velocity, pressure and temperature, respectively. The dimensionless temperature is defined as $\theta=(T-T_0)(T_w-T_0)$, where T_w is the wall/body temperature and T_0 is a reference temperature. In (2.2), $\eta\mathbf{f}$ represents the virtual force only applied to solids. $P_2\theta\mathbf{e}_z$ is the buoyancy with the direction of gravity being $-\mathbf{e}_z$. In (2.3), ηq represents the virtual heat source term only applied to solids to achieve desired temperature distribution of the solid object which will further imposes wanted thermal boundary conditions on fluids. The dimensionless parameters P_1, P_2 and P_3 in (2.2)-(2.3) are defined differently later depending on whether the convection is forced, natural or mixed. For forced convection without buoyancy, $P_1=1/\mathrm{Re}$, $P_2=0$ and $P_3=1/\mathrm{RePr}_x$ where Re and Pr_x are Reynolds number and Prandtl number, respectively. The subscript x in Pr_x denotes its dependence of position $\boldsymbol{x}$, since thermal diffusivity $\alpha(\boldsymbol{x})=\eta(\boldsymbol{x})\alpha_s+(1-\eta(\boldsymbol{x}))\alpha_f$, with α_s and α_f being the thermal diffusivity for solid and fluid respectively. Though thermal diffusivity is requested to be a function of position considering realistic energy transport within solid and fluid domains, kinematic viscosity ν is not requested to be so, since solid is treated as fluid with the idea of virtual forcing under the framework of DFIB. For natural convection in which buoyancy is important, $P_1=\mathrm{Pr}$, $P_2=\mathrm{RaPr}$ and $P_3=\alpha(\boldsymbol{x})/\alpha_f$, where Ra is Rayleigh number. Note that Pr and Ra here again do not have to be functions of position $\boldsymbol{x}$ under the frame work of DFIB, and they are chosen to be based on α_f here. However P_3, considering the realistic heat transport, will depend on position $\boldsymbol{x}$ as the case of forced convection. As to the mixed convection (forced convection with buoyancy considered), it is basically same as forced

https://doi.org/10.4208/cicp.151214.250515s Published online by Cambridge University Press

convection above (without buoyancy) with P_2 set to $\mathrm{Gr}/\mathrm{Re}^2$ instead of 0, where Gr is the Grashof number.

Generally speaking, for solid-fluid conjugate heat transfer, $\alpha(\boldsymbol{x}) = \eta(\boldsymbol{x})\alpha_s + (1-\eta(\boldsymbol{x}))\alpha_f$, and virtual heat source ηq is not required. For solid to provide isothermal boundary condition for fluid, $\alpha(\boldsymbol{x})$ is same as above, but ηq, acting as virtual heat source here, will be nontrivial to uphold constant temperature within solid. For solid to provide insulating boundary condition for fluid, $\alpha(\boldsymbol{x})$ is same as above, but with α_s set to zero throughout the solid domain to uphold no heat flux condition. Under this circumstance, ηq will be trivial here.

2.2 Numerical method

Laminar flows are considered in this study, so no turbulence model is used in the following procedures. A staggered grid arrangement is utilized in this study. That is, pressure and temperature are located at the center of the computational cell while the velocities are placed at the faces of the cell. We use the time-splitting schemes to advance velocity and temperature in (2.2)-(2.3). First, the velocity and temperature are advanced from the m^{th} time level to the first intermediate level "*" by solving the advection-diffusion equations without pressure and virtual force f in (2.2) and the virtual heat source q in (2.3). This step can be stated as the following

$$\frac{\mathbf{u}^* - \mathbf{u}^m}{\Delta t} = S^m - P_2\theta^m \mathbf{e}_z, \tag{2.4}$$

$$\frac{\theta^* - \theta^m}{\Delta t} = H^m, \tag{2.5}$$

where $S = -\nabla\cdot(\mathbf{u}\mathbf{u}) + P_1\nabla^2\mathbf{u}$ and $H = -\nabla\cdot(\mathbf{u}\theta) + P_3\nabla^2\theta$ discretized by the second-order upwind scheme for the convection term and central difference schemes for the diffusion term. Subsequently, we use the second-order Adams-Bashforth method for the temporal discretization with S^m and H^m expressed by

$$S^m = \frac{3}{2}\left(-\nabla\cdot(\mathbf{u}\mathbf{u}) + P_1\nabla^2\mathbf{u}\right)^m - \frac{1}{2}\left(-\nabla\cdot(\mathbf{u}\mathbf{u}) + P_1\nabla^2\mathbf{u}\right)^{m-1}, \tag{2.6}$$

and

$$H^m = \frac{3}{2}\left(-\nabla\cdot(\mathbf{u}\theta) + P_3\nabla^2\theta\right)^m - \frac{1}{2}\left(-\nabla\cdot(\mathbf{u}\theta) + P_3\nabla^2\theta\right)^{m-1}. \tag{2.7}$$

Viscous and diffusion terms in (2.2) and (2.3) can be alternatively treated by implicit scheme like Crank-Nicolson method, which has the advantage of allowing a larger time step, when Reynolds number is small. However, since the Reynolds number of many interesting heat convection problems is often moderate or high and therefore the time step constraint is dominated by CFL condition, here we just use the explicit scheme stated

https://doi.org/10.4208/cicp.151214.250515s Published online by Cambridge University Press

above to save overhead cost of solving Helmholtz equation at each time step due to Crank-Nicolson scheme.

The first intermediate velocity $\mathbf{u}^*$ in (2.4), in general, does not satisfy the divergence-free condition in (2.1). At the second step, we advance the first intermediate velocity by the pressure term

$$\frac{\mathbf{u}^{**}-\mathbf{u}^*}{\Delta t}=-\nabla p^{m+\frac{1}{2}}, \tag{2.8}$$

and apply the divergence to both sides. (2.8) becomes

$$\frac{\nabla\cdot\mathbf{u}^{**}-\nabla\cdot\mathbf{u}^*}{\Delta t}=-\nabla^2 p^{m+\frac{1}{2}}. \tag{2.9}$$

By imposing

$$\nabla\cdot\mathbf{u}^{**}=0, \tag{2.10}$$

we achieve the pressure Poisson equation

$$\nabla^2 p^{m+\frac{1}{2}}=\frac{1}{\Delta t}\nabla\cdot\mathbf{u}^*. \tag{2.11}$$

Once (2.11) is solved, we can advance from $\mathbf{u}^*$ to $\mathbf{u}^{**}$. Conventionally, this would be the end of projection method and actually $\mathbf{u}^{**}=\mathbf{u}^{m+1}$. It is so indeed for a pure fluid cell ($\eta=0$). However, for a cell fully or partially occupied by solids ($\eta>0$), we need one more step to uphold the velocity to be the same as that of solid, say $\mathbf{U}_s$, that is known in advance. This is accomplished by the virtual force applied only to solid part and stated as follows

$$\frac{\mathbf{u}^{m+1}-\mathbf{u}^{**}}{\Delta t}=\eta\mathbf{f}^{m+\frac{1}{2}}, \tag{2.12}$$

with

$$\mathbf{u}^{m+1}=\eta\mathbf{U}_s^{m+1}+(1-\eta)\mathbf{u}^{**}, \tag{2.13}$$

and virtual force $\mathbf{f}^{m+1/2}$ can be determined reciprocally. Taking a cell fully occupied by solid ($\eta=1$) in the case of flow past a still cylinder as an example, then $\mathbf{u}^{m+1}=\mathbf{U}_S^{m+1}=0$. The $\mathbf{f}^{m+1/2}$ calculated by (2.12) will be the virtual force to hold the cell still. Otherwise, pressure gradient generated by (2.11) will cause a nontrivial velocity there. We may imagine that the particles composing the cylinder would be drifted away without a force holding it. Likewise, we need to compensate the solid temperature to a desired distribution by the virtual heat source term, for example in the case of isothermal boundary condition with θ_S known in advance, and this gives the following step in advancing θ^* to θ^{m+1}:

$$\frac{\theta^{m+1}-\theta^*}{\Delta t}=\eta q^{m+\frac{1}{2}}, \tag{2.14}$$

https://doi.org/10.4208/cicp.151214.250515s Published online by Cambridge University Press

with

$$\theta^{m+1}=\eta\theta_S^{m+1}+(1-\eta)\theta^*, \tag{2.15}$$

and virtual heat source $q^{m+1/2}$ can be determined reciprocally too. Again taking cold flow past a still hot cylinder with the surface temperature of cylinder requested to be $\theta=1$ all the time, this boundary condition is equivalent to maintaining the temperature of whole cylinder to be $\theta=1$ all the time. We would then set the initial thermal condition to be $\theta=\eta$. Once the heat convection is on, solid cells would be inevitably cooled and can no more maintain $\theta=1$ without any compensated heat source. The virtual heat source $\eta q^{m+1/2}$ plays exactly the role of heat compensation required.

The integration of virtual force will be a good approximation of the resultant force exerted on the solid object by fluid,

$$\mathbf{F}=-\iiint_{CV}\eta\mathbf{f}dV, \tag{2.16}$$

which is otherwise needed to be calculated by messy surface integration of shear stress and pressure in traditional methods. Easiness of obtaining the resultant force exerted on solid is a chief advantage of the current method, which has not been fully noticed and explored by previous DFIB methods. Likewise, the volume integral of virtual heat source ηq gives us the privilege to determine the net heat rate applied to solid easily, which can further determine Nusselt number by energy balance. In traditional way and case of isothermal boundary condition, once the temperature field is obtained, the local Nusselt number on the solid surface is evaluated using

$$\mathrm{Nu}_s=\frac{\partial\theta}{\partial n}\Big|_{\partial\Omega}, \tag{2.17}$$

where n is the normal direction of the solid surface [24]. Afterward, surface-average Nusselt number becomes

$$W\cdot\overline{\mathrm{Nu}}=\iint_{\partial\Omega}\mathrm{Nu}_s ds=\iiint_{\Omega}\eta q DV, \tag{2.18}$$

where W is the total surface area of the solid object. Obviously without the further equality to the volume integral of virtual heat source in (2.18), evaluating (2.17) and the surface integral in (2.18) would be messy in computation.

In summary, the numerical procedure of the current method at each time step is given below:

1. Determine η through the position and orientation of the solid rigid object.
2. Calculate $\mathbf{u}^*$ and θ^* via (2.4) and (2.5).
3. Solve the Poisson equation (2.11) and advance to $\mathbf{u}^{**}$ via (2.8).

https://doi.org/10.4208/cicp.151214.250515s Published online by Cambridge University Press

4. Update the solid velocity to the prescribed value and compute the virtual force required.
5. Update the solid temperature to the prescribed value and compute the virtual heat source required.

One may argue that the step 4 above after the projection method (step 3) to uphold the physical solid velocity, may destroy the otherwise divergence-free situations throughout the whole domain. It turns out that the divergence-free situation is indeed destroyed in cut cells at which the solid-fluid interface is located. This may imply non-physical mass sources or sinks could be generated in cut cells. Interestingly, these minute sources and sinks come in pairs in cut cells and end up canceling each other to maintain an overall mass conservation. This explains why the scheme still performs well in the benchmarking computations. In fact, when viewing fluid-solid interaction under the framework of immersed interface method, jumps of pressure and velocity derivatives exist when crossing solid-fluid interface [39]. These weak singularities due to jumps happening at interface do mathematically accommodate the violation of divergence-free situation over there if viewing solid and fluid as a whole domain. Implementing virtual force (step 4) after projection (step 3) is also the main difference between our DFIB method and other earlier DFIB methods such as Fadlun *et al.* [14], in which virtual-force step is implemented before projection step to make sure divergence-free situation is obeyed everywhere at the end of each time step. However, this wrong ordering, caused by misconcept about divergence-free situation, would destroy the physical solid velocity upheld in virtual force step. In case of flow past a still cylinder as an example, the cylinder actually would drift due to though small but non-zero velocity at immersed boundary. However, Fadlun *et al.* [14] argued that the drift is very small in their framework.

The current scheme is formally 2nd order accurate in time and space as expressed in (2.4)-(2.12) and (2.14). However, an accuracy degradation will inevitably happen here at cut cells, because the no-slip boundary condition is not exactly upheld at solid-fluid interface. Unlike the DFIB method by Fadlun *et al.* [14] emphasizing to extrapolate the fluid velocity into solid to fit the exact no-slip boundary condition on solid-fluid interface and maintain 2nd order of accuracy in space thoroughly, (2.13) in the sense of weighted average is instead implemented here to determine the velocities in cut cells. This will degrade the order of accuracy to be super-linear (order of accuracy between 1 and 2). However, though the current scheme will not achieve 2nd order of accuracy, it will not either generate spurious internal flow inside the solid object that happens when conducting extrapolation mentioned above. Besides, as a silver lining, resultant force of solid can then be easily obtained by (2.16) here. Volume integral of virtual force using extrapolation will not be equal to the resultant force because of the generation of a non-physical flow inside the solid. It is a worthy trade-off with accuracy for the convenient computation of resultant force. Though above is argued for the momentum equations, similar reasoning can be applied to its energy equation counterpart as well. Besides, implementation of 2nd order approach above inevitably needs to consider full geometric details of

https://doi.org/10.4208/cicp.151214.250515s Published online by Cambridge University Press

each cut cell, and therefore larger overhead in computation would come with that. This is endurable when solid is still since just doing once, but will be costly in time when solid is moving.

3 Results and discussions

3.1 Validation – Forced convection over a heated circular cylinder with an isothermal surface

To validate the established immersed boundary model, we first simulate forced convection over a heated circular cylinder placed in an unbounded uniform flow. The geometric set up in the computational domain and the associate physical boundary conditions are shown in Fig. 1. The Dirichlet boundary condition, i.e. a uniform velocity profile, is applied at the inlet boundary and Neumann boundary conditions are applied at lateral and outlet sides. The incoming fluids are cold ($\theta=0$) whereas the cylinder is considered as a heated body with an isothermal surface ($\theta=1$). Non-uniform rectangular grids (220×180)

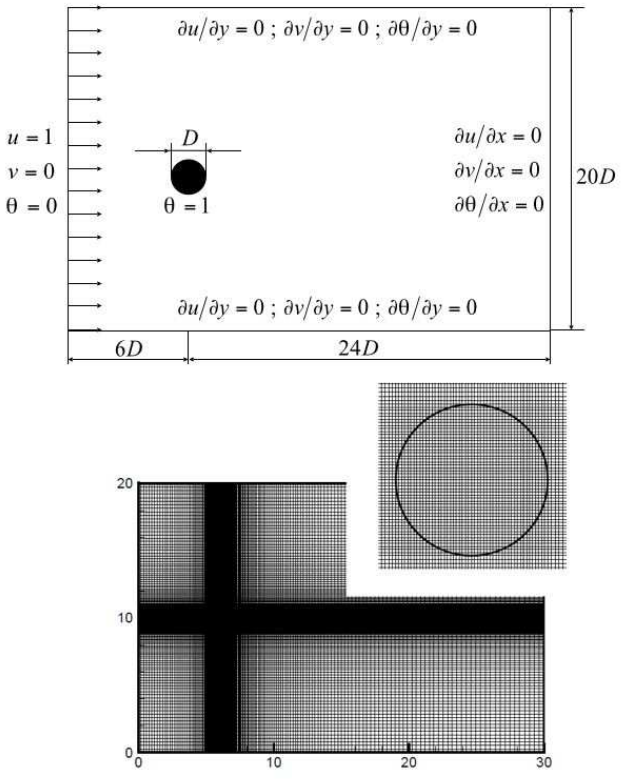


Figure 1: Computational domain, boundary conditions and grids.

https://doi.org/10.4208/cicp.151214.250515s Published online by Cambridge University Press

allocated by a sinusoidal distribution proposed by Kuyper *et al.* [25] is adopted to discretize the computational domain, with a uniform grid (50×50) is employed to cover the cylinder (Fig. 1). A grid independence study is undertaken using various grids such as 100×90, 150×130, and 220×180. In terms of the predicted wake length, results are very close. Therefore, the grids (220×180) should be enough to obtain grid independent solutions.

Simulations have been conducted for a variety of Reynolds numbers based on the cylinder diameter and the free stream velocity. Streamlines, vorticity contours and isotherm contours for simulation at Re = 40 and Re = 100 are shown in Figs. 2 and 3, respectively. It is well known that at low Re, the flow pattern remains symmetric with a pair of stationary re-circulating vortices behind the cylinder (see Fig. 2). Increasing Re leads to instability of flow structures, so a pair of symmetrical vortices behind cylinder breaks down and the vortex starts to shed up and down alternatively (see Fig. 3). This shedding frequency can be revealed as a dimensionless parameter, namely Strouhal number. The re-circulation length (x_r), drag coefficient (C_D), Strouhal number (St) and Nusselt number (Nu) are compared with some previous works and presented in Table 1. In general, all results obtained by the established model show good agreements with those previous studies.

Table 1: The comparison of average drag coefficients, recirculation length and Strouhal numbers at Re = 40 and 100.

	Re = 40			Re = 100			
	C_D	x_r	$\overline{\text{Nu}}$	C_D	C_L	St	$\overline{\text{Nu}}$
Tritton (experiment) [32]	1.48	-	-	1.25	-	-	-
Borthwick [33]	1.507	-	-	1.215	-	-	-
Sheard *et al.* [34]	1.5	-	-	1.38	-	-	-
Dennis and Chang [35]	1.522	2.35	-	1.056	-	-	-
Lange *et al.* [36]	1.5	-	3.28	1.319	-	0.165	5.00
Soares *et al.* [37]	1.49	2.275	3.20	-	-	-	-
Fornberg [38]	1.498	2.24	-	1.058	-	-	-
Lai and Peskin [10]	-	-	-	1.4473	±0.3229	0.165	-
Su [11]	1.63	-	-	1.4	-	0.168	-
Ye [13]	1.52	2.27	-	-	-	-	-
Tseng and Ferziger [15]	1.53	2.21	-	1.42	±0.29	0.164	-
Vega [22]	1.53	2.28	3.62	-	-	-	-
Pan [23]	1.51	2.18	3.23	1.32	±0.32	0.16	5.02
Kim *et al.* [26]	1.51	-	-	1.33	±0.32	0.165	-
Ecker and Soehngen [27]	-	-	3.48	-	-	-	-
Dias and Majumdar [28]	1.54	2.69	-	1.395	±0.283	0.171	-
Present study	1.567	2.219	3.32	1.4	±0.322	0.167	5.08

https://doi.org/10.4208/cicp.151214.250515s Published online by Cambridge University Press

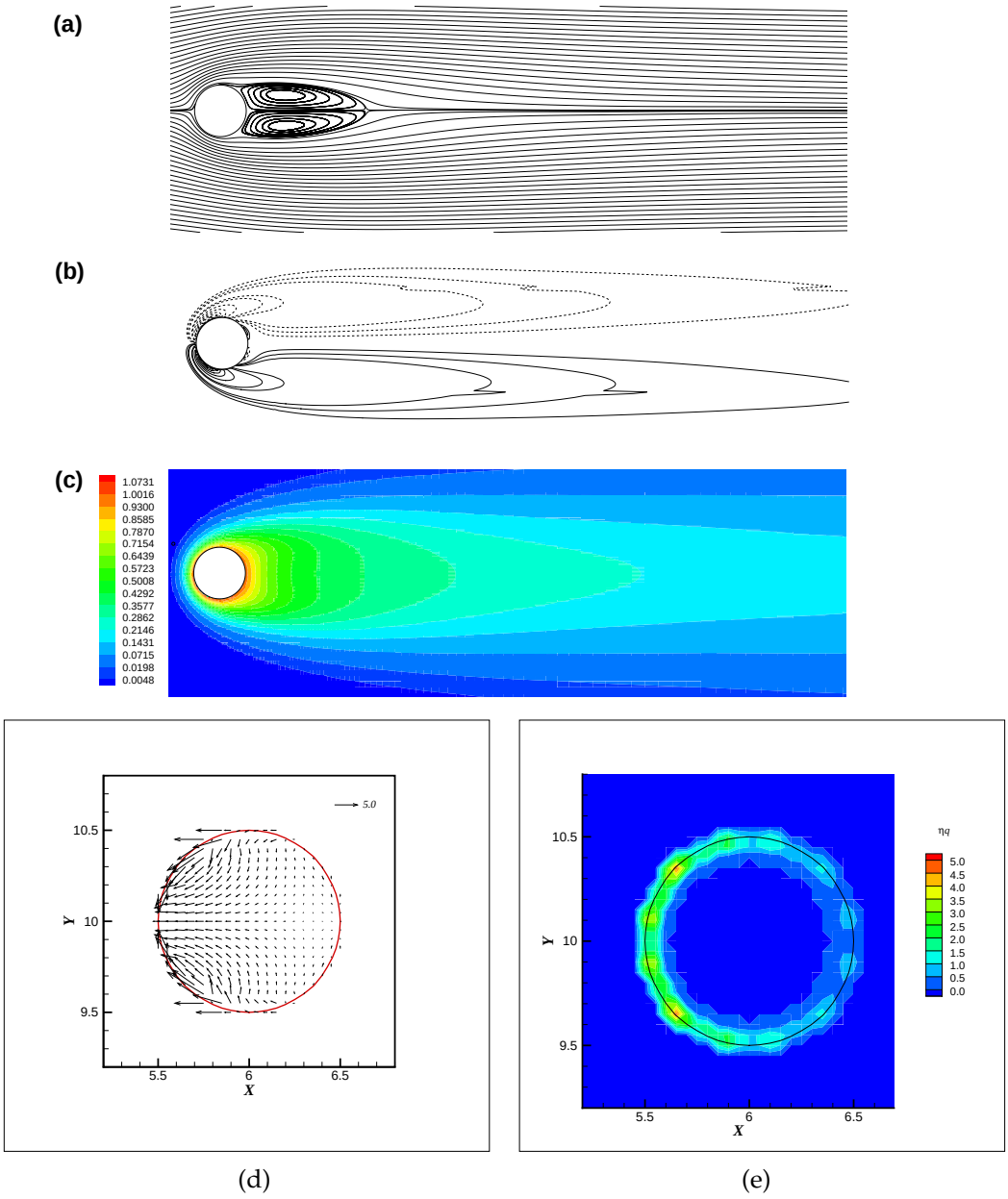


Figure 2: (a) Streamlines, (b) vorticity contours, (c) isotherms, (d) $\eta\mathbf{f}$ and (e) ηq at Re $=$ 40.

Since virtual force and heat source are the main features of current method, their distributions are particularly demonstrated in Figs. 2(d) and (e) for the case of Re $=40$. In Fig. 2(d) $\eta\mathbf{f}$ is plotted when the flow becomes steady, and this distribution is mainly to compensate for the velocity caused by the pressure gradient from (2.9) so that the

https://doi.org/10.4208/cicp.151214.250515s Published online by Cambridge University Press

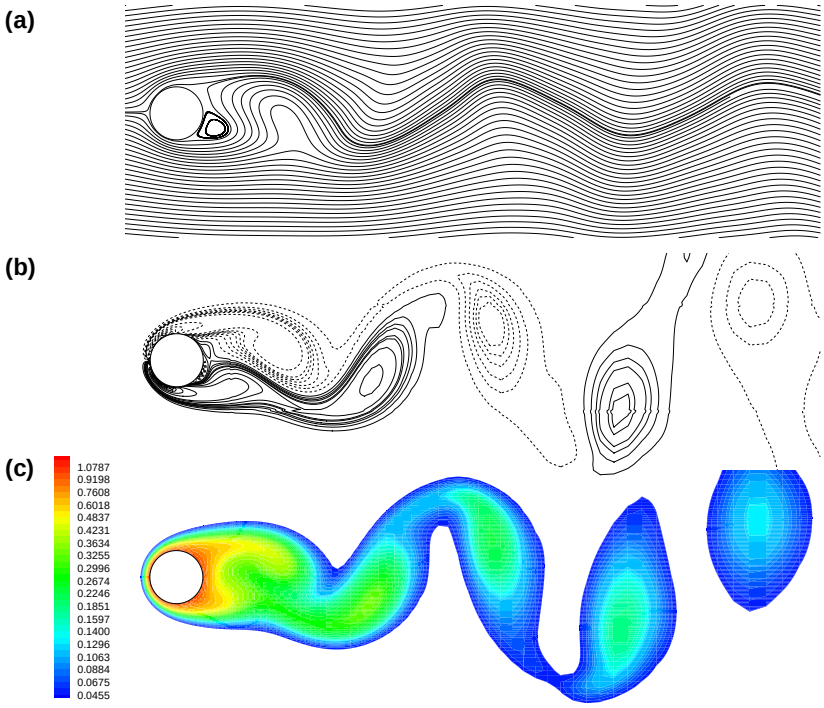


Figure 3: (a) Streamlines, (b) vorticity contours and (c) isotherms at Re = 100.

resultant velocity is zero inside the cylinder. In Fig. 2(e), the counterpart of Fig. 2(d), ηq is plotted, and this distribution is to compensate the cooling caused by the incoming cold flow so that the temperature of whole cylinder can be maintained to be $\theta = 1$, and therefore isothermal boundary condition can be upheld. One can see virtual force and heat source both have larger distribution at the up-wind side than the lee side due to larger pressure and stronger cooling respectively.

3.2 Natural convection in a square enclosure with a heated circular cylinder

The established immersed boundary model is further applied to simulations of natural convection in a square enclosure with a heated circular cylinder placed at its center. Due to the temperature difference between the hot cylinder and cold ambient fluid, buoyancy is induced and causes an upward flow. The system consists of a square enclosure of length L whereas the diameter of the cylinder is $D = 0.2L$. The walls of the square enclosure are kept at a constant low temperature of θ_C while the cylinder is kept at another constant high temperature of θ_H. We define L, θ_C and θ_H as the characteristic length, the reference temperature and the wall temperature, respectively. The computational domain as well as the boundary conditions are shown in Fig. 4. 201×201 uniform Cartesian grids are employed in the computational domain.

https://doi.org/10.4208/cicp.151214.250515s Published online by Cambridge University Press

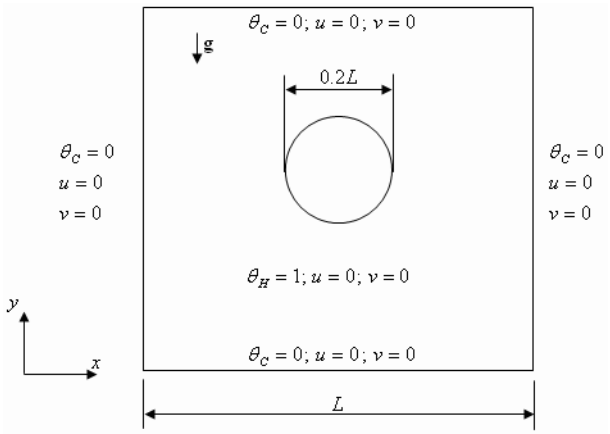


Figure 4: Computational domain and the coordinate system along with boundary conditions.

The isotherms and streamline contours for simulations at Ra $=10^4$, 10^5 and 10^6 are presented in Fig. 5. For the case at Ra $=10^4$, the heat transfer inside the enclosure is mainly dominated by heat conduction. At the higher Ra of 10^5, the thermal plume commences to appear on the top of the cylinder due to the buoyancy. The thermal gradient at the upper part of the enclosure is much stronger than the lower one. Consequently, the dominant flow is found in the upper half of the enclosure. It indicates that natural convection plays an important role in flow and thermal field inside the enclosure. As Ra increases to 10^6, the heat transfer in the enclosure is mainly by natural convection. The thermal plume strongly impinges on the top of the enclosure to form a thinner thermal boundary layer and enhances the heat transfer.

The surface averaged Nusselt numbers $\overline{\text{Nu}}$ of the cylinder for different Ra are given in Table 2. $\overline{\text{Nu}}$ of the cylinder increases as Ra increases due to the domination of convective heat transfer. To study the effect of fractional values of η, we perform simulations

Table 2: $\overline{\text{Nu}}$ around a circular cylinder placed concentrically inside an enclosure, $D=0.2L$. The terms A and B indicate that the calculations are performed by ignoring and including fractional values of η, respectively. η will be only either 0 or 1 for A and $0<\eta<1$ for B.

	Ra $=10^4$	Ra $=10^5$	Ra $=10^6$
Moukalled and Archarya [29]	2.071	3.825	6.107
Shu *et al.* [30]	2.082	3.786	6.106
101 101 A	2.100	3.767	5.837
101 101 B	2.065	3.550	5.245
151 151 A	2.109	3.839	6.077
151 151 B	2.107	3.835	6.070
201 201 A	2.079	3.813	6.108
201 201 B	2.078	3.812	6.106

https://doi.org/10.4208/cicp.151214.250515s Published online by Cambridge University Press

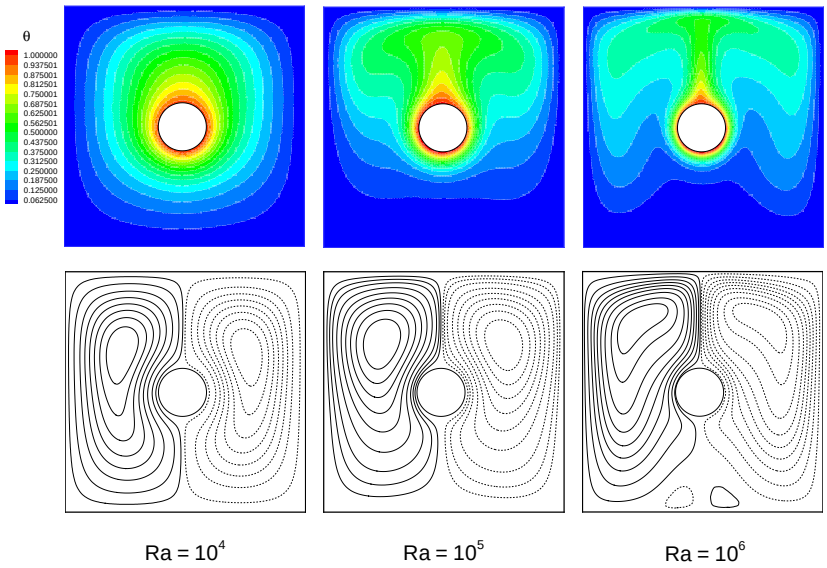


Figure 5: Isotherms (upper) and streamlines (lower) of natural convection in a square enclosure with a circular cylinder, $D=0.2L$. The cylinder is at the center of the enclosure.

for two different types of grids, i.e. A and B as shown in Table 2. The terms A and B indicate that the calculations are performed by ignoring and including fractional values of η, respectively. η is either 0 or 1 only for A and $0\leq\eta\leq1$ for B. In terms of our results, it is observed that the difference of calculation $\overline{\text{Nu}}$ between A and B is not significant when simulations are preformed using more grids. Furthermore, we choose uniform 201×201 grids for all simulations in the following cases. Also, again the present results in Table 2 agree well with literatures [29,30].

To further validate the proposed method, we also undertake simulations for natural convection over a heated cylinder placed eccentrically inside a square enclosure. The cylinder has a diameter $D=0.2L$. Its center is located at $(x,y)=(-0.15L,-0.15L)$ from the center of the enclosure. This case is common and has been studied by other scholars. The isotherm and streamline contours at different Ra are presented in Fig. 6 whereas the comparison of the average Nusselt number with previous studies is given in Table 3. Again, the present results show good agreement with previous studies [22,23,31].

Table 3: $\overline{\text{Nu}}$ around a circular cylinder placed eccentrically inside an enclosure, $D=0.2L$.

	Ra $=10^4$	Ra $=10^5$	Ra $=10^6$
Vega *et al.* [22]	4.750	7.519	12.531
Pan [23]	4.686	7.454	12.540
Sadat and Couturier [31]	4.699	7.430	12.421
Present study	4.712	7.481	12.523

https://doi.org/10.4208/cicp.151214.250515s Published online by Cambridge University Press

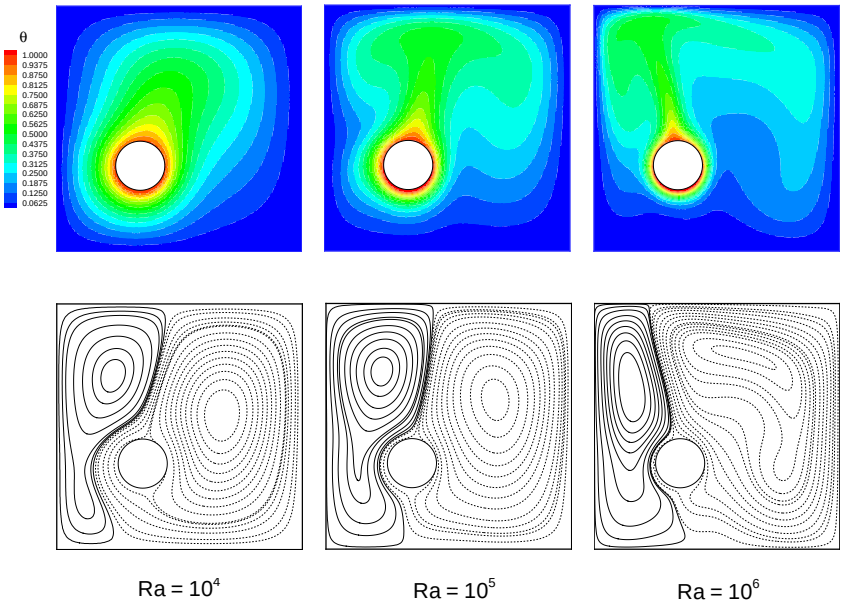


Figure 6: Isotherms (upper) and streamlines (lower) of natural convection in a square enclosure with a circular cylinder, $D=0.2L$. The cylinder is not at the center of the enclosure.

3.3 Natural convection in a square enclosure with a moving heated circular cylinder

To further demonstrate the capability of the present DFIB in handling fluid-solid interactions with a moving hot object, we perform the simulations of natural convection in a square enclosure with a moving heated circular cylinder. The cylinder has a diameter $D=0.2L$, where L is the length of the square enclosure. The cylinder sways sinusoidally in the horizontal direction with the amplitude of $A=0.5D$ as shown in Fig. 7 and the non-dimensional swaying frequency ϖ is equal to 1. The instantaneous displacement d of the cylinder from its mean position is given by $d=A\sin(\varpi t)$. The cylinder is at the center of the square enclosure initially. The simulation is performed till it reaches a periodic phenomenon. The instantaneous streamline, isotherm and vorticity contours during a cycle are shown in Fig. 8. It should be noted that thermal physical properties of fluid in this case are as same as the case of natural convection at Ra $=10^6$. It is found that the thermal plume, which also occurs in a stationary cylinder case, is again shown in Fig. 8 sweeping above the cylinder due to the sway of the cylinder. The thermal plume plays a vital role in the heat dispersion as already shown in Table 3. It is interesting to know the effect of the cylinder motion on the behavior of the thermal plume and the heat dispersion from the cylinder. In the case of horizontally moving cylinder (Fig. 8), two main eddies due to the thermal plume occupy the entire enclosure. The sizes of those two counter rotating eddies change periodically due to their interaction with the cylinder.

https://doi.org/10.4208/cicp.151214.250515s Published online by Cambridge University Press

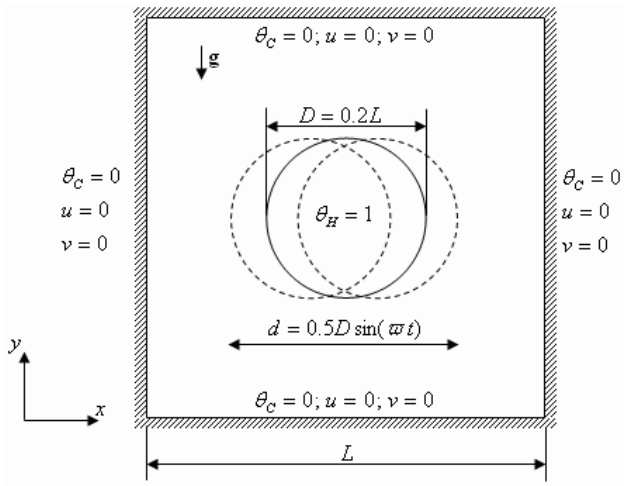


Figure 7: Computational domain and the coordinate system along with boundary conditions for mixed-convection in a square enclosure with a moving heated circular cylinder.

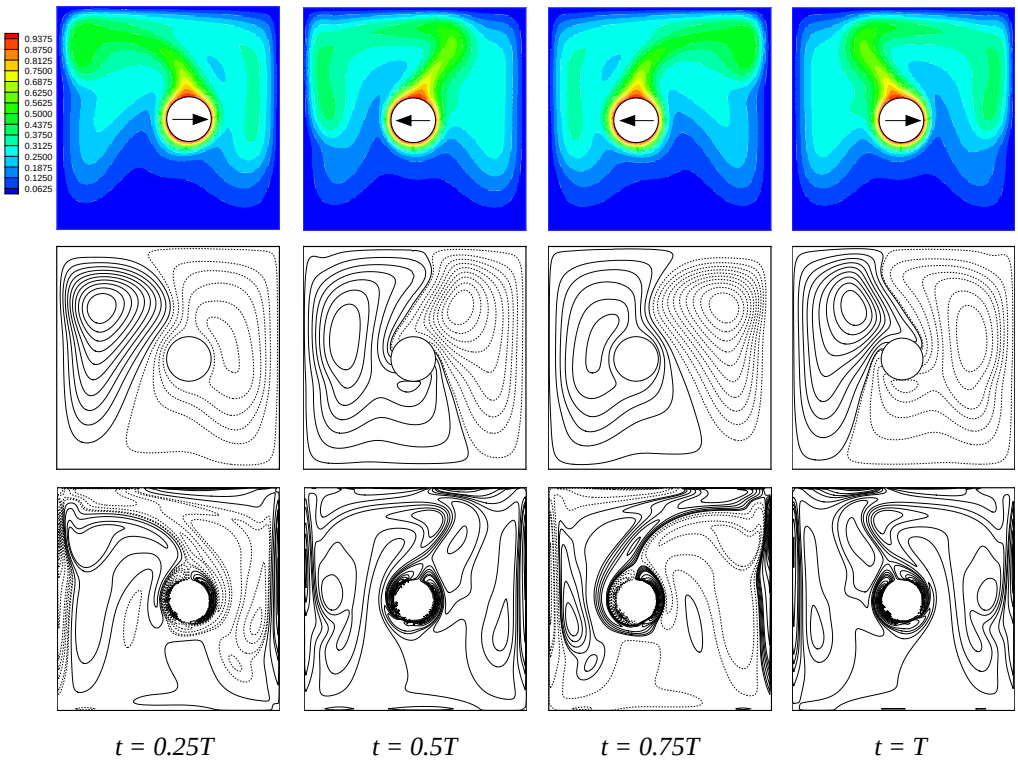


Figure 8: Snapshots of isotherms (upper) streamline (middle) vorticity (lower) contours during a cycle of horizontal swaying, $\varpi = 1$, $A = 0.5D$.

https://doi.org/10.4208/cicp.151214.250515s Published online by Cambridge University Press

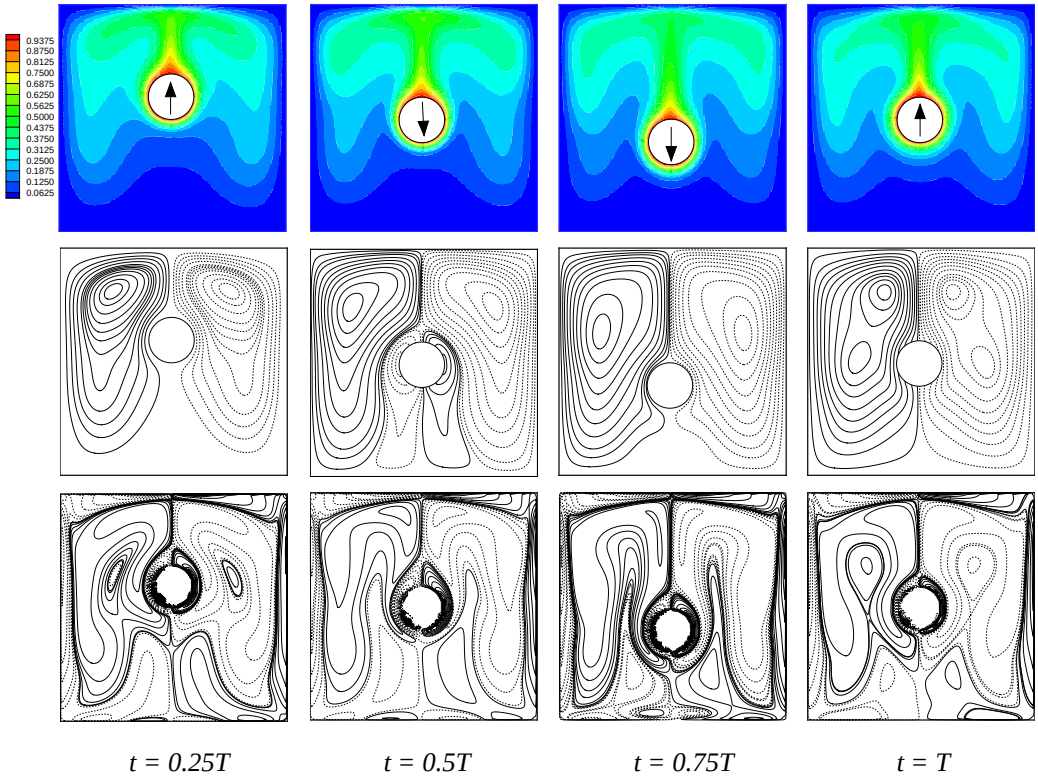


Figure 9: Snapshots of isotherms (upper) streamline (middle) vorticity (lower) contours during a cycle of vertical bouncing, $\omega=1$, $A=0.5D$.

In addition to the sway of the cylinder, the vertical motion of the cylinder, which is in the direction of the gravity is also worthy of investigation. Hence, the simulation which considers a cylinder bouncing up and down is undertaken at Ra $=10^6$. Snapshots of the instantaneous isotherm, streamline and vorticity contours during a cycle are presented in Fig. 9. It turns out that isotherms, streamlines and vorticity patterns are always symmetric with respect to the gravitational direction. Sizes of those two main eddies vary due to the bouncing motion, but they are not distorted like the sway case.

In addition to swaying and bouncing cylinders, we extend our simulation by combining those motions, i.e. the cylinder moving in a counter-clockwise circular orbit which is concentric with the enclosure and has the radius R. Such a movement stirs the flow inside the enclosure in a more complicated way and may further cause more complicated patterns in the natural convection. The description of this problem is given in Fig. 10. The isotherm, streamline and vorticity contours during a cycle are given in Fig. 11 with $\omega=1$. It is found that the thermal plume is distorted due to the orbital motion. Those two main eddies still exist and are disturbed by the moving cylinder. They are distorted and their sizes vary due to the horizontal and the vertical movements in the orbital motion.

https://doi.org/10.4208/cicp.151214.250515s Published online by Cambridge University Press

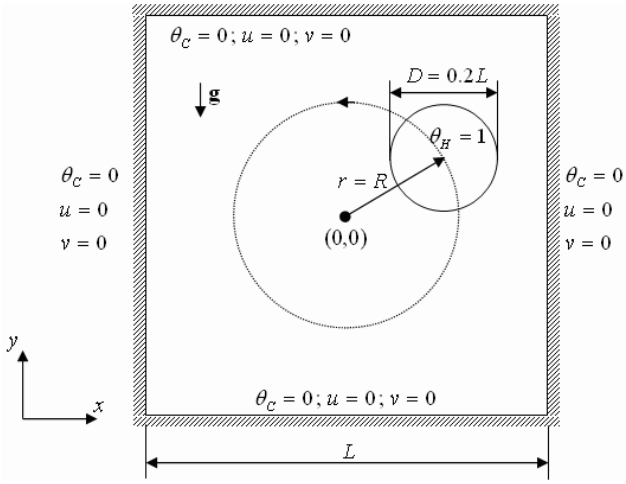


Figure 10: Computational domain and the coordinate system along with boundary conditions for mixed-convection in a square enclosure with a heated circular cylinder moving in a counter-clockwise orbit.

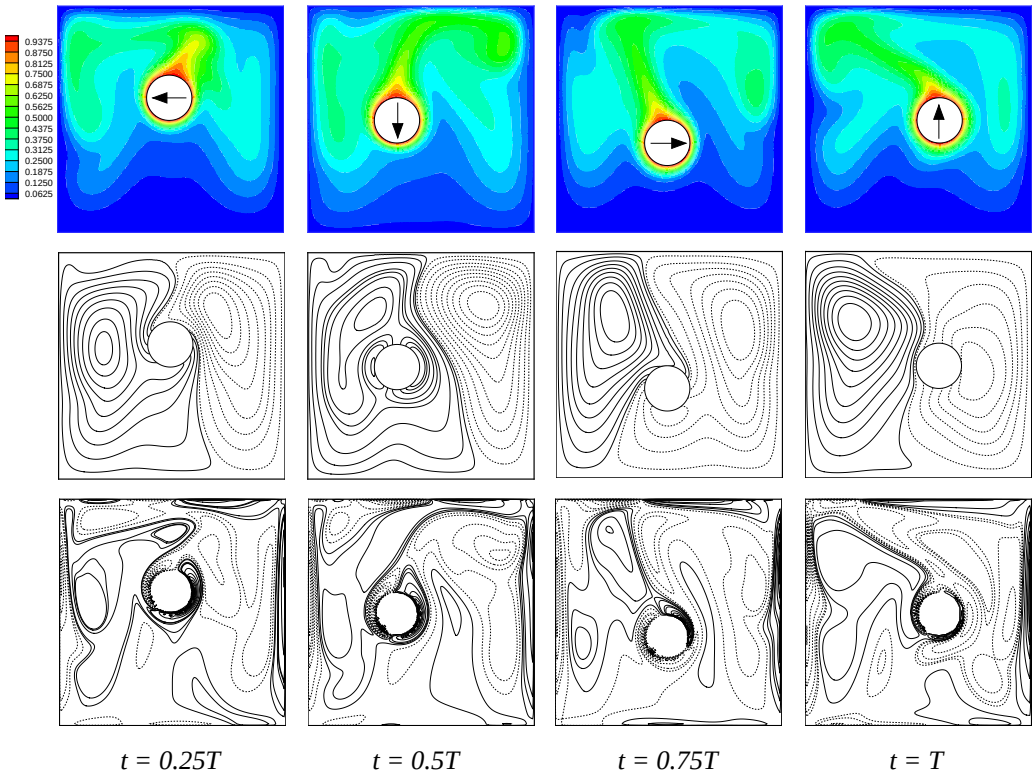


Figure 11: Snapshots of isotherms (upper) streamline (middle) vorticity (lower) contours during a period of movement in a counter-clockwise orbit, $R=0.5D$, $\omega=1$.

https://doi.org/10.4208/cicp.151214.250515s Published online by Cambridge University Press

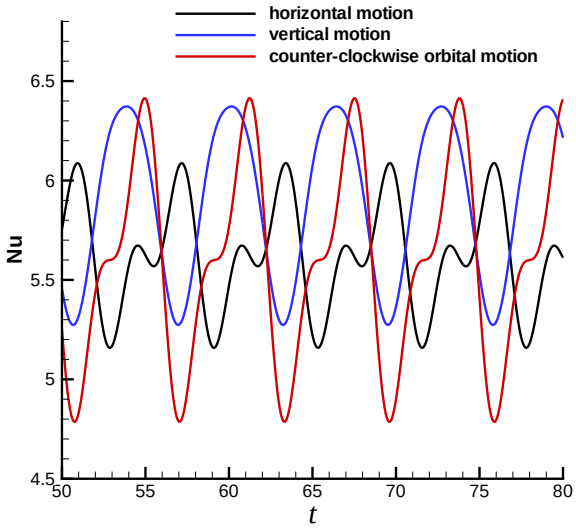


Figure 12: Time histories of $\overline{\text{Nu}}$ for the three cases shown in Figs. 8, 9 and 11.

Together with the previous cases, we show the time histories of $\overline{\text{Nu}}$ for those three cases (Figs. 8, 9 and 11) at Ra $= 10^6$ and present them in Fig. 12. For the considered amplitude (A) and oscillating frequency of cylinder motion (ω), it can be observed that $\overline{\text{Nu}}$ for moving objects are lower than the case of the stationary one in Table 3 (due to larger plum development space in Table 3) and also lower than that in Table 2 for most of time. When the hot cylinder starts to move in any direction, it sheds convective cells which are induced by the thermal plume above the heated cylinder. These cells spread heat to the adjacent fluid. After one period, while the convective cells keep growing, the cylinder moves toward its starting position and penetrates the growing hot region, the heat transfer form the hot cylinder to the fluid is consequently reduced. To further observe these phenomena, we perform the simulations at different amplitudes (A) and oscillating frequencies (ω) of the cylinder motion. We calculated and tabulate the time average of $\overline{\text{Nu}}$ in Table 4. When the amplitude is very small, e.g. $A=0.005D$, the cylinder

Table 4: Time average of $\overline{\text{Nu}}$ of a moving circular cylinder at different amplitude and oscillating frequency, $D=0.2L$.

Motion	ω	$A=0.005D$	$A=0.05D$	$A=0.5D$
Horizontal	0.1	6.117	6.111	6.062
Horizontal	1.0	6.114	6.083	5.628
Vertical	0.1	6.130	6.125	6.110
Vertical	1.0	6.127	6.103	5.912
Orbital	0.1	6.122	6.120	6.079
Orbital	1.0	6.118	6.085	5.639

https://doi.org/10.4208/cicp.151214.250515s Published online by Cambridge University Press

acts as a slightly vibrating object. For all the cases in Table 4, we observe that the highest time-averaged $\overline{\mathrm{Nu}}$ is found at the smallest amplitude, $A = 0.005D$. On the other hand, smaller oscillating frequencies offer higher time-averaged $\overline{\mathrm{Nu}}$ due to the slower motion of the cylinder, which spends more time for convective cells spreading heat before the cylinder moves back. It should be noted that all cases were computed and compared to stationary natural convection at $\mathrm{Ra} = 10^6$ (as shown in Table 2) with fluid and thermal properties being the same. The flow is more dominated by natural convection than by the forced cylinder motion. Hence, the motion of cylinder does not offer any significant effect to increase heat transfer between the hot cylinder and the fluid.

4 Conclusions

A modified DFIB method is established in this study to explore interactions of fluids and structures both in mechanics and heat transfer. The fraction of solid at each computational cell is determined. Subsequently, it is involved in the computation of the virtual force and heat source. The virtual force and heat source are added into the momentum and energy equation to realize the effects of solids on the flow and heat transfer via the role of an immersed body, respectively. The current method is validated by a uniform flow past a heated circular cylinder. Good agreements are found in flow characteristics and heat transfer features between the present model and previous studies. Furthermore, the natural convection in a square enclosure with a heated cylinder inside is simulated by the proposed model. The surface-average Nusselt number for the hot cylinder is calculated and agrees well with previous studies. The established DFIB model is also able to consider a moving solid object. The cylinder inside the square enclosure is forced to move to test the capability of the current method. The circular cylinder sways, bounces and moves in a circular orbit in the square enclosure. Influences of the motion of the cylinder on the natural convection inside the enclosure are observed from the calculated data. Consequently, the proposed DFIB method here is able to simulate both mechanics and heat transfer in fluid-solid interaction problems.

Acknowledgments

This work is supported in part by the Ministry of Science and Technology of Taiwan (Grants No. MOST 103-2212-E-011-110-MY3 and MOST 103-2115-M-035-001).

References

[1] C. W. Hirt, A. A. Amsden and J. L. Cook, An arbitrary Lagrangian-Eulerian computing method for all flow speeds, J. Comput. Phys., 4 (1974), 227-253.

https://doi.org/10.4208/cicp.151214.250515s Published online by Cambridge University Press

[2] D. Bailey, M. Berndt, M. Kucharik and M. Shashkov, Reduced-dissipation remapping of velocity in staggered arbitrary Lagrangian-Eulerian methods, J. Comput. Appl. Math. 233 (2010), 3148-3156.
[3] M. Kucharik, R. Liska, M. Shashkov, Conservative Remapping and ALE Methods for Plasma Physics, in Proceedings of HYP 2004, Tenth International Conference on Hyperbolic Problems: Theory, Numerics, Applications, Yokohama Publisher, Japan, 2006.
[4] D. J. Benson, Computational methods in Lagrangian and Eulerian hydrocodes, Comput. Method Appl. M., 99 (1992), 235-394.
[5] P. Kjellgren and J. Hyvarinen, An arbitrary Lagrangian-Eulerian finite element method. Comput. Mech., 21 (1998), 81-90.
[6] J. S. Peery and D. E. Carrol, Multi-material ALE methods in unstructured grids, Comput. Method Appl. M., 187 (2000), 591-619.
[7] C. S. Peskin, Flow patterns around heart valve: A numerical method, J. Comput. Phys., 10 (1972), 252-271.
[8] D. Goldstein, R. Handler and L. Sirovich, Modeling and no-slip flow boundary with an external force field, J. Comput. Phys., 105 (1993), 354-366.
[9] E. M. Saiki and S. Biringen, Numerical simulation of a cylinder in uniform flow: Application of a virtual boundary method, J. Comput. Phys., 123 (1996), 450-365.
[10] M. C. Lai and C. S. Peskin, An immersed boundary method with formal second-order accuracy and reduced numerical viscosity, J. Comput. Phys., 160 (2000), 705-719.
[11] S. W. Su, M. C. Lai and C. A. Lin, An immersed boundary technique for simulating complex flows with rigid boundary, Comput. Fluids, 36 (2007), 313-324.
[12] J. Mohd-Yusof, Interaction of massive particles with turbulence, PhD. Dissertation, Dept. of Mechanical and Aerospace Engineering, Cornell University, USA, 1996.
[13] T. Ye, R. Mittal, H. S. Udaykumar and W. Shyy, An accurate Cartesian grid method for viscous incompressible flows with complex immersed boundaries, J. Comput. Phys., 156 (1999), 209-240.
[14] E. A. Fadlun, R. Verzicco, P. Orlandi and J. Mohd-Yusof, Combined immersed-boundary finite-difference method for three dimensional complex flow simulations, J. Comput. Phys., 161 (2000), 35-60.
[15] Y. H. Tseng and J. H. Ferziger, A ghost-cell immersed boundary method for flow in complex geometry, J. Comput. Phys., 192 (2003), 593-623.
[16] N. Zhang and Z. C. Zheng, An improved direct-forcing immersed-boundary method for finite difference applications, J. Comput. Phys., 221 (2007), 250-268.
[17] D. Z. Noor, M. J. Chern and T. L. Horng, An immersed boundary method to solve fluid-solid interaction problems, Comput. Mech., 44 (2009), 447-453.
[18] M. J. Chern, W. C. Hsu and T. L. Horng, Numerical prediction of hydrodynamic loading on circular cylinder array in oscillatory flow using direct-forcing immersed boundary method, J. Appl. Math., (2012), Article ID 505916.
[19] M. J. Chern, W. C. Shiu and T. L. Horng, Immersed boundary modeling for interaction of oscillatory flow with cylinder array under effects of flow direction and cylinder arrangement, J. Fluid Struct., 43 (2013), 325-346.
[20] M. J. Chern, Y. H. Kuan, G. Nugroho, G. T. Lu and T. L. Horng, Direct-forcing immersed boundary modeling of vortex-induced vibration of a circular cylinder, J. Wind Eng. Ind. Aerod., 134 (2014), 109-121.
[21] F. Paravento, M. J. Pourquie, B. J. Boersma, An immersed boundary method for complex flow and heat transfer, Flow Turbul. Combust., 80 (2007), 187-206.

https://doi.org/10.4208/cicp.151214.250515s Published online by Cambridge University Press

[22] A. P. Vega, J. R. Pacheco and T. Rodic, A general scheme for the boundary conditions in convective and diffusive heat transfer with immersed boundary methods, J. Heat Transf., 129 (2007), 1506-1516.
[23] D. Pan, An immersed boundary method on unstructured Cartesian meshes for incompressible flows with heat transfer, Numer. Heat Tr. B-Fund., 49 (2006), 277-297.
[24] S. D. Dhole, R. P. Chhabra and V. Eswaran, A numerical study on the forced convection heat transfer from an isothermal and isoflux sphere in the steady symmetric flow regime, Int. J. Heat Mass Tran., 49 (2006), 984-994.
[25] R. A. Kuyper, T. H. van der Meer, C. J. Hoogendoorn and R. A. W. M. Henkes, Numerical study of laminar and turbulent natural convection in an inclined square cavity, Int. J. Heat Mass Tran., 36 (1993), 2899-2911.
[26] J. Kim, D. Kim and H. Choi, An immersed-boundary finite-volume method for simulations of flow in complex geometries, J. Comput. Phys., 171 (2001), 132-150.
[27] E. R. G., Eckert and E. Soehngen, Distribution of heat transfer coefficients around circular cylinder in cross flow at Reynolds number from 20 to 500, Trans. ASME, 74 (1952), 343347.
[28] A. Dias and S. Majumdar, Numerical computation of flow around a circular cylinder, Technical Report, PS II Report, BITS Pilani, India, 2002.
[29] F. Moukalled and S. Acharya, Natural convection in the annulus between concentric horizontal circular and square cylinder, J. Thermophys. Heat Tr., 10 (1996), 524-531.
[30] C. Shu, H. Xue, Y. D. Zhu, Numerical study of natural convection in an eccentric annulus between a square outer cylinder and a circular inner cylinder using DQ method, Int. J. Heat Mass Tran., 44 (2001), 3321-3333.
[31] H. Sadat and S. Couturier, Performance and accuracy of a meshless method for laminar natural convection, Numer. Heat Tr. B-Fund., 37 (2000), 455-467.
[32] D. J. Tritton, Experiments on the flow past a circular cylinder at low Reynolds number, J. Fluid Mech., 6 (1959), 547-567.
[33] A. G. L. Borthwick, Comparison between two finite difference schemes for computing the flow around a cylinder, Int. J. Numer. Methods Fluids, 6 (1986), 275-290.
[34] G. J. Sheard, K. Hourigan and M. C. Thompson, Computations of the drag coefficients for low-Reynolds-number flow past rings, J. Fluid Mech., 526 (2005), 257-275.
[35] S. C. R. Dennis and G. Z. Chang, Numerical solutions for steady flow past a circular cylinder at Reynolds numbers up to 100, J. Fluid Mech., 42 (1970), 471-489.
[36] C. F. Lange, F. Durst and M. Breuer, Momentum and heat transfer from cylinders in laminar crossflow at $10^{-4} \leq Re \leq 200$, Int. J. Heat Mass Tran., 41 (1998), 3409-3430.
[37] A. A. Soares, J. M. Ferreira and R. P. Chhabra, Flow and forced convection heat transfer in crossflow of non-Newtonian fluids over a circular cylinder, Industrial & Engineering Chemistry Research, 44 (2005), 5815-5827.
[38] B. Fornberg, A numerical study of steady viscous flow past a circular cylinder, J. Fluid Mech., 98 (1980), 819-855.
[39] Z. Li and M. C. Lai, The immersed interface method for the NavierStokes equations with singular forces, J. Comput. Phys., 171 (2001), 822-842.

https://doi.org/10.4208/cicp.151214.250515s Published online by Cambridge University Press